Title: Clonal spreading of tumor-infiltrating T cells underlies the robust antitumor immune responses

Authors:

Hiroyasu Aoki[1,2,4], Mikiya Tsunoda[1], Haru Ogiwara[1], Haruka Shimizu[1], Haruka Abe[1], Takaya Abe[3], Shigeyuki Shichino[1], Kouji Matsushima[1], Satoshi Ueha[1,4,*]

Affiliations:

[1]Division of Molecular Regulation of Inflammatory and Immune Diseases, Research Institute for Biomedical Sciences, Tokyo University of Science, Noda city, Chiba, 278-8510, Japan

[2]Department of Hygiene; Graduate School of Medicine, The University of Tokyo, Bunkyo-ku, Tokyo, 113-0033, Japan

[3]Laboratory for Animal Resources and Genetic Engineering, RIKEN Center for Biosystems Dynamics Research, Chuo-ku, Kobe, Hyogo, 650-0047, Japan

[4]These authors contributed equally

*Satoshi Ueha, Ph.D., Division of Molecular Regulation of Inflammatory and Immune Diseases, Research Institute for Biomedical Sciences, Tokyo University of Science,

2669 Yamazaki, Noda City Chiba, 278-0022, Japan

E-mail; ueha@rs.tus.ac.jp

Abstract

The repertoire of tumor-infiltrating T cells is an emerging perspective for characterizing effective antitumor T-cell responses. Oligoclonal expansion of tumor T-cell repertoire has been evaluated; however, their association with antitumor effects is unclear. We demonstrated that the polyclonal fraction of the tumor-reactive T-cell repertoire consisting of relatively minor clones increased in tumor-bearing mice treated with anti-PD-L1 or anti-CD4 monoclonal antibody, which was correlated with antitumor effect. Meanwhile, the size of the oligoclonal fraction consisting of major clones remained unchanged. Moreover, the polyclonal fraction was enriched in progenitor exhausted T cells, which are essential for a durable antitumor response, and was more dependent on $CCR7^{+}$ migratory dendritic cells, which are responsible for priming tumor-reactive T cells in the tumor-draining lymph nodes. These results suggest that the expansion of diverse tumor-reactive clones ("clonal spreading") is an important mechanism by which anti-PD-L1 and anti-CD4 treatments induce robust and durable antitumor T-cell responses.

Keywords: TCR repertoire**,** tumor-infiltrating T cells, dLN-tumor overlap, polyclonal fraction, clonal spreading, anti-PD-L1 mAb, anti-CD4 mAb, progenitor exhausted T cells,

40 migratory DC

41

42 **Introduction**

43 Immune checkpoint inhibitors (ICIs), including programmed cell death-1 (PD-
44 1) inhibitors, are widely used to treat various types of cancer. However, only 20%–30%
45 of patients respond to ICIs[1], and the factors determining the differences between
46 responders and non-responders remain unknown. The differences in clinical responses
47 are not only due to the immune resistance mechanism of the tumor but also due to the
48 strength of the antitumor immune response induced by ICIs[2]. Hence, characterizing the
49 antitumor immune response that leads to better clinical outcomes is critical for
50 optimizing patient selection and developing new therapeutic combinations.

51 $CD8^+$ tumor-infiltrating T-lymphocytes (TILs), the primary effector cells of the
52 antitumor immune response, are composed of various T-cell clones with different
53 antigen specificities determined by T-cell receptors (TCRs)[3–5]. TCR transgenic mice[6]
54 and peptide-major histocompatibility complex (MHC) multimer technology[7] have been
55 used in several pre-clinical and clinical studies to analyze the characteristics of a small
56 set of clones with high affinity to tumor antigens. More recently, TCR sequencing, a
57 global analysis of TCRs using next-generation sequencing, has enabled the analysis of a
58 collection of T-cell clones and the TCR repertoire[8,9]. Hence, the TCR repertoire has
59 been used to investigate the features of antitumor T-cell responses, leading to better

60 therapeutic effects.

61 The TCR repertoire of TILs is highly skewed toward a small number of clones,
62 in which the top 1% of the most abundant clones result in more than 20% of the TILs,
63 suggesting the expansion of tumor-reactive clones[10,11]. Thus, the features of the TCR
64 repertoire of TILs have been evaluated using the clonality index[12], representing the
65 extent to which a part of the T-cell clones expanded in the repertoire ("clonal skewing").
66 Indeed, a higher clonality is associated with antitumor effects[10,13–15]. T-cell clones that
67 encounter antigens and proliferate in tumors differentiate into a dysfunctional state
68 called exhaustion[16–18]. In contrast, the TIL subpopulations associated with a good
69 response to anti-PD-1 mAb treatment are less exhausted and moderately expanded in
70 tumors[19]. Thus, T-cell responses in which diverse tumor-reactive clones expand
71 moderately ("clonal spreading") are also expected to exert a desirable antitumor effect.
72 However, the contribution of clonal spreading to the antitumor immune response has not
73 been intensively studied.

74 T-cell clones that recognize epitopes unrelated to tumors also infiltrate the
75 tumor tissue and form medium- and low-frequency clones ("bystander" clones)[20]. Thus,
76 to assess the clonal spreading of tumor-reactive T cells, it is important to distinguish the
77 medium- and low-frequency tumor-reactive clones from bystander clones. T-cell clones

78 present in both tumor-draining lymph nodes (dLNs) and tumors (dLN-tumor
79 overlapping (OL) clones) are considered to be enriched in tumor-reactive clones that are
80 primed in the dLN and trafficked into the tumor via blood circulation[21,22]. Considering
81 that the newly emerged TIL clones replace exhausted clones during the anti-PD-1
82 therapy[23], the overlapping TIL clones supplied by the dLNs seem to play a central role
83 in anti-tumor T cell responses. We have previously demonstrated that an anti-CD4
84 monoclonal antibody (anti-CD4 mAb), which exerts potent antitumor effects in mice
85 and humans by depleting $CD4^+$ cells, including regulatory T cells (Tregs), and
86 activating tumor-reactive $CD8^+$ T-cell responses[24–27], significantly increased the number
87 and total frequency of dLN-tumor OL clones. However, it was unclear whether the
88 increase in dLN-tumor repertoire overlap was also observed with PD-1 blockade and a
89 combination of anti-CD4 and anti-PD-L1 mAbs (hereafter designated as
90 "CD4+PDL1"), which exert synergistic anti-tumor effect[24]. Furthermore, it remains
91 unclear whether this increase in the frequency of dLN-tumor OL clones is due to clonal
92 skewing or spreading.
93 Here, we performed a T-cell receptor repertoire analysis of B16F10 and Lewis
94 lung carcinoma tumor-bearing mice treated with anti-PD-L1 and anti-CD4 mAbs. By
95 analyzing the dLN-tumor OL repertoire, we demonstrated that the number of TIL clones

96 supplied by dLNs increased after anti-PD-L1 and anti-CD4 treatment owing to clonal
97 spreading rather than clonal skewing. Moreover, the greater extent of clonal spreading
98 in anti-CD4 and CD4+PDL1 combination treatment was correlated with their superior
99 anti-tumor effects.
100
101 **Results**
102 **Anti-PD-L1 and anti-CD4 treatments increased the dLN-tumor repertoire overlap**
103 **in a B16 melanoma model**
104 In our previous study, we demonstrated that anti-CD4 treatment increases the
105 total frequency of dLN-tumor OL $CD8^+$ T-cell clones[25]. Moreover, in the first-in-human
106 trial, anti-CD4 treatment increased the tumor-associated T-cell clones in the peripheral
107 blood, which was associated with the anti-tumor effects[27]. To examine whether the
108 increase in the dLN-tumor repertoire overlap also occurs in anti-PD-L1 treatment or in
109 CD4+PDL1 combination treatment, we analyzed the TCR repertoire of B16F10 tumor-
110 bearing mice treated with anti-PD-L1 mAb, anti-CD4 mAb, and CD4+PDL1 treatments
111 (Fig. 1a). In this model, the anti-CD4 and CD4+PDL1 treatments caused an antitumor
112 effect on day 13, while the anti-PD-L1 treatment did not (Fig. 1b and c). The TCR
113 repertoire of $CD44^{hi}$ $CD8^+$ T cells in the dLN and $CD8^+$ T cells in the tumor was analyzed

114 on day 14 after tumor inoculation (Fig. 1d). We then identified the dLN-tumor OL clones
115 and compared their total frequency among the treatment groups (Fig. 1f and g). The
116 treatment with anti-CD4 mAb and CD4+PDL1 significantly increased the total frequency
117 of OL clones in the dLN and tumors (Fig. 1h and i). The anti-PD-L1 treatment
118 significantly increased the total frequency of OL clones in the tumor to a lesser extent
119 (Fig. 1i). These results suggest that both the anti-PD-L1 and anti-CD4 treatments
120 enhanced the mobilization of tumor-reactive clones in the antitumor T-cell response.

121 The clonality of the TCR repertoire, which is the extent of clonal skewing in
122 tissues, are commonly evaluated to monitor the antitumor T-cell responses[12]. In the dLN
123 repertoire, clonality increased in the anti-CD4 and CD4+PDL1 groups, consistent with
124 the increase in the dLN-tumor repertoire overlap (Supplementary Fig. 1a). In contrast,
125 clonality did not change in the tumor repertoire between the treatment groups with
126 different antitumor responses (Supplementary Fig. 1a). This suggests that in the B16
127 model, the dLN-tumor repertoire overlap reflects the effect of immunotherapies on the
128 tumor T-cell repertoire more clearly than the commonly used clonality index.

129

130 **Clonal spreading was prominent in the dLN-tumor repertoire overlap following**
131 **anti-PD-L1 and anti-CD4 treatments**

132 Next, we examined whether the increase in the dLN-tumor repertoire overlap
133 following the anti-PD-L1 and anti-CD4 treatments was due to clonal skewing or clonal
134 spreading of the tumor-reactive clones. For this purpose, dLN-tumor OL clones were
135 categorized into “top 10 clones” or “11th-or-lower clones” according to their frequency
136 in the tumor and were considered to belong to the “oligoclonal” or “polyclonal” fraction,
137 respectively (Fig. 2a and b). The total frequencies of oligoclonal and polyclonal overlap,
138 which reflect the clonal skewing and spreading, respectively, were compared between the
139 treatment groups (Fig. 2c). Oligoclonal overlap tended to increase following anti-PD-L1
140 or anti-CD4 treatment; however, the differences were not statistically significant. In
141 contrast, polyclonal overlap increased significantly in the anti-PD-L1, anti-CD4, and
142 CD4+PD-L1 groups (Fig. 2d). We also classified the clones into major (> 1%),
143 intermediate (0.1%–1%), and minor clones (< 0.1%) based on their frequency within the
144 tumor and confirmed that CD4 and PD-L1 expanded the polyclonal OL clones
145 (Supplementary Fig. 1b and c). Similar results were observed in the Lewis lung carcinoma
146 (LLC) tumor model: the polyclonal overlap increased in the treated groups, whereas the
147 oligoclonal overlap was the same as that in the control (Supplementary Fig. 1d). These
148 results demonstrate that the increase in the dLN-tumor repertoire overlap was mainly due
149 to the clonal spreading of tumor-reactive T cells rather than clonal skewing.

150 To clarify the association between clonal spreading and the antitumor effects of
151 immunotherapies, we calculated the correlation between the tumor volume on day 13 and
152 the oligoclonal or polyclonal fraction of the dLN-tumor OL repertoire (Fig. 2e).
153 Polyclonal overlap was more strongly correlated with the tumor volume than oligoclonal
154 overlap. A stronger correlation between the polyclonal overlap and tumor volume was
155 also observed in the LLC model (Supplementary Fig. 1e). These results suggest that the
156 clonal spreading of tumor-reactive T cells induced by the anti-PD-L1 and anti-CD4
157 treatments enhances the antitumor T-cell responses, leading to therapeutic effects.
158

159 **The polyclonal fraction of the dLN-tumor OL repertoire was enriched with**
160 **progenitor-like exhausted T cells**

161 $CD8^+$ TILs display a dysfunctional state called exhaustion, which is
162 characterized by a high expression of inhibitory receptors such as PD-1 or T-cell
163 immunoglobulin and mucin-domain containing-3 (TIM-3)[18]. Tumors contain two subsets
164 of exhausted T cells: terminally exhausted T cells are characterized by a high expression
165 of inhibitory receptors and exhibit high tumor reactivity, while progenitor exhausted T
166 cells are characterized by improved persistence and a self-renewal capacity[28–31]. Because
167 progenitor exhausted T cells can proliferate and generate terminally exhausted ones

168 following PD-1 blockade, this subset is thought to be essential for a durable antitumor T-
169 cell response[29]. Based on these findings, we then investigated whether the progenitor
170 exhausted cells corresponded to a polyclonal fraction of the dLN-tumor OL repertoire,
171 which reflects clonal spreading.

172 To answer this question, single-cell targeted RNA sequencing and TCR
173 sequencing (scRNA/TCRseq) were performed using a BD Rhapsody system (Fig. 3a).
174 $CD8^+$ TILs were collected from B16F10 tumor-bearing mice treated with anti-CD4 mAb,
175 and a library was generated for scRNA/TCRseq. Out of the 12,397 cells analyzed, paired
176 TCR sequences were detected in 10,649 cells (pairing efficiency, 85.9%). Eight clusters
177 were identified based on the single-cell gene expression profiles (Fig. 3b and
178 Supplementary Fig. 2a). Based on the expression levels of marker genes (Fig. 3c and
179 Supplementary Fig. 2b) and the gene expression signature scores (Fig. 3D and
180 Supplementary Fig. 2c), we characterized these clusters as "naïve (NV)-like" (#7),
181 "progenitor exhausted" (#4 and 6), and "terminally exhausted" (#0, 1, 2, 3, and 5). Among
182 the "progenitor exhausted" clusters, cluster 4 showed an intermediate level of exhaustion
183 scores and a lower expression level of *Tcf7*, suggesting an intermediate state between
184 progenitor exhausted and terminally exhausted states (Fig. 3c and d). These findings were
185 supported by the result of pseudotime analysis, which revealed the trajectory from cluster

186 7 (NV-like) through clusters 4 and 6 (progenitor exhausted) to clusters 0 and 1 (terminally
187 exhausted) (Supplementary Fig. 2b). Among the "terminally exhausted" clusters, cluster
188 2 was highly proliferative and cluster 3 was more cytotoxic, according to the *Gzma*
189 expression level and the cytotoxicity score (Supplementary Fig. 2c and d). Moreover,
190 cluster 5 was characterized by a high expression of interferon-responsive genes, such as
191 *Isg15* and *Mx1* (Fig. 3c and Supplementary Fig. 2d). The clonality of the "terminally
192 exhausted" clusters was higher than the "progenitor exhausted" and "NV-like" clusters,
193 showing that the "terminally exhausted" clusters were composed of highly expanded
194 clones (Supplementary Fig. 2e).

195 To compare the phenotype of the T-cell clones consisting of the oligoclonal and
196 polyclonal fractions of the dLN-tumor OL repertoire, we identified the OL clones using
197 the results of bulk TCR-seq performed on dLN $CD8^{+}$ $CD44^{high}$ T cells collected from the
198 same mouse (Fig. 3a). Oligoclonal or polyclonal OL clones were projected onto a uniform
199 manifold approximation and projection (UMAP) plot (Fig. 3e, left). The oligoclonal and
200 polyclonal fractions of the dLN-tumor OL repertoire contained very few cells from the
201 "NV-like" cluster (#7), which supported the tumor reactivity of the OL clones. The
202 proportion of "terminally exhausted" clusters (#0, 1, 2, 3, and 5) was over 50% in the
203 oligoclonal and polyclonal overlap. At the same time, the proportion of "progenitor

204 exhausted" clusters (#4 and 6) was higher in the polyclonal fraction (5.2% in the
205 oligoclonal fraction vs. 27.6% in the polyclonal fraction; Fig. 3e, right). Consistently, the
206 polyclonal fraction was predominant in the "progenitor exhausted" clusters (Fig. 3f and
207 Supplementary Table S1). Moreover, the genes representing the progenitor- and
208 terminally exhausted phenotypes were highly expressed in the polyclonal and oligoclonal
209 fraction, respectively (Supplementary Fig. 2f). At the clone level, a higher frequency of
210 OL clones in the tumor was associated with a lower score for the progenitor exhausted
211 state and a higher score for the terminally exhausted state (Fig. 3g). These results
212 demonstrate that the oligoclonal OL mainly consisted of terminally exhausted T cells,
213 while the polyclonal fraction of the dLN-tumor OL repertoire was enriched in progenitor
214 exhausted T cells.
215

216 **The polyclonal fraction of the OL repertoire was dominant in the Ly108^{+} Tim-3^{-} TIL**
217 **subpopulation**

218 To confirm the results of the scRNA/TCRseq analysis in a high-throughput
219 manner, we performed bulk TCR repertoire analysis on the CD8^{+} TIL subpopulations at
220 different exhaustion stages. Using Tim-3 and Ly108 as cell surface markers for progenitor
221 and terminally exhausted T cells[29,31], the CD8^{+} TILs from B16F10 tumor-bearing mice

222 treated with anti-PD-L1 and anti-CD4 were sorted into PD1$^-$, PD1$^+$ Ly108$^+$ Tim-3$^-$
223 ("Ly108"), PD1$^+$ Ly108$^+$ Tim-3$^+$ ("DP"), and PD1$^+$ Ly108$^-$ Tim-3$^+$ ("Tim-3") subsets
224 using flow cytometry (Fig. 4a). Among these subpopulations, T-cell exhaustion is thought
225 to progress in the following order: PD1$^-$, Ly108, DP, and Tim-3[29]. We then analyzed the
226 TCR repertoire of these four TIL subsets as well as CD44^{hi} CD8$^+$ T cells in the dLN. The
227 clonality of the TCR repertoire was the lowest in PD1$^-$ and gradually increased in the DP
228 and Tim-3 subsets in anti-CD4-treated mice (Fig. 4b). A similar tendency was observed
229 in the anti-PDL1 and CD4+PDL1 groups (Supplementary Fig. 3a). These results show
230 that the repertoire of the PD1$^-$ and Ly108 subsets was more polyclonal than that of DP
231 and Tim-3, consistent with the scRNA/TCRseq analysis results (Supplementary Fig. 2d).
232 Next, we attempted to verify whether the polyclonal overlap predominated in the
233 progenitor exhausted population. For this purpose, we estimated the frequency of each
234 clone in the total CD8$^+$ TILs ("pooled") by estimating the frequency within the TIL
235 subsets (PD1$^-$, Ly108, DP, and Tim-3) weighted by the total cell count of these subsets
236 (Fig. 4c, example). We confirmed that the frequency of each clone in the pooled repertoire,
237 which was estimated as described previously, was correlated with the frequency in the
238 real CD8$^+$ TIL repertoire (Supplementary Fig. 3b). Subsequently, the OL clones in the
239 oligoclonal and polyclonal fractions were identified based on their frequency in the

240 pooled $CD8^+$ TIL repertoire (Fig. 4c), and their total frequency in each T-cell subset was
241 calculated ($PD1^-$, Ly108, DP, and Tim-3). In the anti-CD4 group, the proportion of the
242 oligoclonal fraction was significantly higher in the DP and Tim-3 subsets than in the $PD1^-$
243 and Ly108 subsets, while that of the polyclonal fraction was the highest in the Ly108
244 subset (Fig. 4d). Consistently, the proportion of the polyclonal fraction surpassed that of
245 the oligoclonal fraction in Ly108 cells (Fig. 4e). These results confirmed the findings of
246 the scRNA/TCRseq analysis that the oligoclonal fraction predominated among terminally
247 exhausted T cells, while the polyclonal fraction contained more progenitor exhausted T
248 cells in the dLN-tumor OL repertoire. Notably, the CD4+PDL1 group exhibited results
249 similar to those of the anti-CD4 group; however, this tendency was not observed in the
250 anti-PDL1 group (Supplementary Fig. 3c and d). This may reflect a weaker degree of
251 clonal spreading in the anti-PDL1 group than in the anti-CD4 or CD4+PDL1 group.
252

253 **Enhanced priming by migratory DCs in the dLN contributed to clonal spreading**
254 **following anti-PD-L1 and anti-CD4 treatments**

255 Our results from the TCR repertoire analysis proposed that the clonal spreading
256 of tumor-reactive T cells contributed to the antitumor effect induced by anti-PD-L1 and
257 anti-CD4 treatments in the B16F10 model. As for the mechanism of clonal spreading, we

258 hypothesized that the anti-PD-L1 and anti-CD4 treatments enhanced the priming of more
259 diverse T-cell clones in the dLN. Migratory DCs in the dLN, which deliver tumor antigens
260 and play a critical role in inducing tumor-reactive CD8 T-cell responses[32,33], express a
261 higher level of PD-L1 than resident DCs. Moreover, because Tregs deprive co-stimulatory
262 molecules on migratory DCs through CTLA-4[34], the anti-CD4 treatment, which removes
263 CTLA-4 expressing Tregs, seems to enhance the priming of $CD8^+$ T cells by migratory
264 DCs in the dLN. To examine whether migratory DC-dependent priming contributes to the
265 clonal spreading after the treatment, we utilized $Fscn1^{DTR\text{-}Cre}$ knock-in mice to remove
266 the $CCR7^+$ $FSCN1^+$ migratory DCs in the dLN (Supplementary Fig. 4a). FSCN1 is an
267 actin-bundling protein that promotes the migration of DCs into LNs[35–37]. Since FSCN1 is
268 expressed not only in $CCR7^+$ migratory DCs but also in neurons[35,38], we inoculated
269 B16F10 cells into FSCN1 KI bone marrow chimeric mice (FSCN1 BMC). In tumor-
270 bearing FSCN1 BMC mice, DTR was weakly expressed on a part of $CCR7^+$ MHC II^+
271 DCs in the tumor and strongly expressed on most migratory DCs in the dLN
272 (Supplementary Fig. 4b). Administration of DT to these mice slightly decreased the
273 number of $CCR7^+$ MHC II^+ DCs in the tumor and completely depleted migratory DCs in
274 the dLN (Supplementary Fig. 4c).

275 We subjected B16F10-bearing FSCN1 BMC mice to anti-PD-L1 and anti-CD4

276 treatments, with or without DT administration (Fig. 5a). Depletion of migratory DCs in
277 the dLN of DT-treated mice was confirmed on day 14 (Fig. 5b-d). TCR repertoire analysis
278 revealed that the total frequency of dLN-tumor OL clones in the tumor decreased in mice
279 receiving DT in the anti-PD-L1 and CD4+PD-L1 groups (Fig. 5e). The oligoclonal
280 fraction of the dLN-tumor OL repertoire was equivalent or higher in DT-treated mice
281 compared to DT-untreated mice (Fig. 5f). In contrast, the polyclonal fraction of the dLN-
282 tumor OL repertoire decreased following DT administration in all three treatment groups
283 (Fig. 5g). These results suggest that the anti-CD4 and anti-PD-L1 antibodies enhance the
284 priming of tumor-reactive T-cell clones by migratory DCs in the dLN, leading to clonal
285 spreading in tumor-bearing mice.
286
287 **Discussion**
288 We demonstrated that the anti-PDL1 and anti-CD4 mAb treatment increased the
289 $CD8^+$ T-cell repertoire overlap in the dLN and tumor, mainly owing to clonal spreading.
290 In the B16F10 model, anti-CD4 and CD4+PD-L1 treatments exert strong antitumor
291 effects whereas anti-PD-L1 treatment alone shows a limited antitumor effect[24]. In the
292 present study, the antitumor effect of anti-CD4, anti-PD-L1, and CD4+PD-L1 treatments
293 correlated with the extent of clonal spreading. Single-cell analysis of the gene expression

294 and TCR sequences of TILs revealed that progenitor exhausted T cells, which are
295 essential for a durable antitumor response to PD-1 blockade[29–31], were enriched in a
296 polyclonal fraction of the OL repertoire, which reflected clonal spreading. Furthermore,
297 enhanced priming in the dLN by migratory DCs contributed to the clonal spreading of
298 tumor-reactive clones following anti-PD-L1 and anti-CD4 treatments. These results
299 suggest that clonal spreading induces antitumor T-cell responses by anti-PD-L1 and anti-
300 CD4 treatments in the B16 melanoma model.

301 Our finding that clonal spreading were enhanced after anti-PD-L1 and anti-CD4
302 treatments seems to contradict with many previous studies on the repertoire analysis of
303 TILs reporting an association between oligoclonal expansion and objective antitumor
304 effects following ICIs[10,13–15]. However, these studies did not separate $CD4^+$ and $CD8^+$
305 TILs prior to TCR sequencing. $CD8^+$ TILs exhibit higher clonality than $CD4^+$ TILs[19] in
306 most cases, and the clonality of the total TIL repertoire is reported to be correlated with
307 the proportion of $CD8^+$ cells[39]. This evidence suggests that the higher clonality in these
308 studies reflects a larger proportion of $CD8^+$ cells in TILs. Here, we performed a TCR
309 repertoire analysis of purified $CD8^+$ T cells and clarified the clonal composition changes
310 in the $CD8^+$ T-cell repertoire under immunotherapy, which was not evident in previous
311 studies.

312 TCR repertoire analysis on dLN-tumor repertoire overlap clearly demonstrated
313 that the anti-PD-L1 and anti-CD4 treatments did not increase clonal skewing but
314 enhanced the clonal spreading of tumor-reactive T cells. Notably, the increase in the
315 polyclonal fraction of the TIL repertoire following anti-PD-L1 and anti-CD4 treatments
316 was not observed when non-overlapping clones were included in the analysis. Thus, the
317 analysis of the dLN-tumor OL, which enriches the TIL clones supplied by dLNs, is
318 important for quantifying the clonal spreading of tumor-reactive T cells and evaluating
319 antitumor T cell responses.

320 scTCR analysis of TILs and bulk TCR repertoire analysis of exhausted TIL
321 subsets revealed the immunological phenotypes of the oligoclonal and polyclonal
322 fractions of the dLN-tumor OL repertoire; unfortunately, we could not analyze untreated
323 mice owing to the low density and number of $CD8^+$ TILs in the B16F10 model. Recent
324 studies on the scTCR analysis of human TILs reported that highly expanded $CD8^+$ T cell
325 clones exhibited a terminally exhausted phenotype with tumor reactivity[16,40,41]. Consistent
326 with these findings, the oligoclonal fraction of the dLN-tumor OL also largely consisted
327 of T cells with a terminally exhausted phenotype and contained a small amount of
328 progenitor exhausted T cells. Conversely, the proportion of progenitor exhausted T cells
329 in the polyclonal fraction of dLN-tumor OL was higher than that in the oligoclonal

330 fraction. In addition, Naïve-like and PD1^{-} CD8^{+} TILs with low tumor-reactivity[5] were
331 enriched in the non-OL repertoire but not in the polyclonal fraction of OL, as expected.
332 Considering that terminally exhausted T-cell clones inside the tumor were replaced
333 following PD-1 blockade in cancer patients[23], the OL clones in the polyclonal fraction
334 may function as reserves while oligoclonal fraction may not persist for a long period.
335 Furthermore, it is also presumed that clonal spreading owing to anti-PD-L1 and anti-CD4
336 treatments enlarges the reservoir of tumor-reactive T-cell clones, which underlies the
337 robust and persistent antitumor effect.

338 One question that remained unaddressed was how the anti-PD-L1 and anti-CD4
339 treatments enhance the clonal spread of tumor-reactive T cells. We initially hypothesized
340 that the enhanced priming of tumor-reactive clones in the dLN increases the polyclonal
341 fraction of the dLN-tumor OL repertoire. Indeed, in mouse models, the activation of T
342 cells in the dLN is enhanced by anti-CD4[24] and anti-PD-L1 treatments[42]. The priming of
343 tumor-reactive T cells in the dLN is mainly mediated by CCR7^{+} migratory DCs, which
344 capture tumor antigens, mature in the tumor, and migrate to the dLN via lymphatics[32,33].
345 Migratory DCs express a higher level of PD-L1, whose interactions with PD-1 on
346 activated CD8^{+} T cells is inhibited by PD-1 blockades in the dLN[42]. Moreover, the anti-
347 CD4 treatment, which removes CTLA-4 expressing Tregs, may promote the priming of

348 $CD8^+$ T cells through increasing the expression of CD80/86 on migratory DCs in the dLN.
349 These observations support the possibility that clonal spreading is promoted by the
350 enhanced priming capacity of migratory DCs. In line with this, the specific depletion of
351 migratory DCs in $FSCN1^{DTR\text{-}Cre}$ KI BMC mice reduced the polyclonal fraction of the
352 dLN-tumor OL repertoire. Our results underscore the contribution of the enhanced
353 priming in the dLN to the clonal spreading of tumor-reactive clones.

354 This study had some limitations. First, we could not demonstrate the relationship
355 between the extent of clonal spreading and clinical outcomes in patients with cancer under
356 ICI treatment. This is attributable to our limited access to the dLN specimen. TCR
357 repertoire analysis on a bilateral subcutaneous tumor model, in which tumor cells are
358 inoculated bilaterally into the backs of mice, could be an alternative approach that provide
359 the evidence for a causal relationship between clonal spreading and the antitumor effect
360 of ICIs[43,44]. Second, we could not analyze the immunological differences between clones
361 contributing to clonal skewing and clonal spreading, including the tumor reactivity, TCR
362 affinity, and exhaustion status. Clones in oligoclonal OL, which are observed in tumor-
363 bearing mice, regardless of the treatment, are thought to exhibit higher affinity for cancer
364 antigens and are able to expand under immune checkpoints but are more prone to
365 exhaustion. Conversely, clones in polyclonal overlap, whose expansion is enhanced by

366 ICIs, are thought to have TCRs with lower affinity for cancer antigens and need more
367 costimulatory signals for expansion[45]. Cloning the TCR alpha- and beta-chain pairs using
368 scTCR sequencing and generating TCR transgenic T cells of various dLN-tumor OL
369 clones would enable us to validate the features and functions of T-cell clones contributing
370 to clonal skewing or clonal spreading. Here, we defined the oligoclonal/polyclonal
371 fraction based on the rank or frequency of clones in the tumor. However, a more refined
372 definition, which incorporates the immunological features of clones, such as the
373 exhaustion status or TCR affinity, can more precisely evaluate the extent of clonal
374 spreading and become a more reliable marker for the treatment outcome.
375 In summary, our results suggest that an enhanced clonal spreading underlies the robust
376 antitumor immune responses by which anti-PD-L1 and anti-CD4 treatments. Overall, we
377 emphasize the importance of evaluating the polyclonal nature of antitumor T-cell
378 responses through TCR repertoire analysis, which provides a novel index that reflects the
379 efficacy of ICI treatments.
380

381 **Methods**

382 **Materials availability**

383 The Fscn1 knockin mouse (Accession No. CDB0153E:

384 https://large.riken.jp/distribution/mutant-list.html) will be distributed upon requests. All
385 antibodies, reagents, oligonucleotides, and software and algorithms used in this study are
386 listed in Supplementary Table S2-5, respectively.

387 **Data and code availability**

388 All sequencing data (Bulk TCRseq, and Single-cell RNA/TCR sequencing) have
389 been deposited at GEO and are publicly available as of the date of publication (GEO:
390 GSE198211).

391 All original code has been deposited at Github (https://github.com/hiro-aoki-
392 mriid/Aoki_ICIrepertoire).

393 **Mice**

394 Eight-week-old female C57BL/6 mice (CD90.2) were purchased from Sankyo
395 Labo service corporation inc. CD90.1 congenic mice with gp100 melanoma antigen-
396 specific Pmel-1 TCR transgene (Pmel Tg, #:005023) were purchased from The Jackson
397 Laboratory, then B6 mice were backcrossed for at least 6 generations. Female Pmel Tg
398 mice were used for the experiment at 8-10 weeks old. All mice were bred at specific
399 pathogen-free facilities in Research Institute for Biomedical Sciences, the Tokyo
400 University of Science and in RIKEN Kobe branch.

401 **Cell lines**

402 Lewis lung carcinoma (LLC) was kindly provided by Dr. Fuminori Abe (Nippon
403 Kayaku). B16F10 is a gp100^{+} spontaneous murine melanoma cell line, kindly provided
404 by Dr. N. Restifo (National Cancer Institute, MD). Both cell lines were cultured in RPMI-
405 1640 medium (Nakarai) supplemented with 10% fetal bovine serum (MP Bio Japan), 1%
406 HEPES (Nakarai) and 1% penicillin/streptomycin (Nakarai) at 37˚C in a humidified
407 atmosphere at 5% CO_2.

408 **Generation of Fscn1DTR-Cre knock-in mice**

409 The Fscn1 knockin mouse (Accession No. CDB0153E:
410 https://large.riken.jp/distribution/mutant-list.html) was generated by CRISPR/Cas9-
411 mediated knockin in zygotes as previously described [46]. For the homologous
412 recombination-mediated knockin, the donor vector consisting of homology arms and
413 P2A-DTR-P2A-Cre (insert gene) was generated to insert the P2A-DTR-P2A-Cre cassette
414 at the 3-base upstream of the PAM sequence. For microinjection, the mixture of crRNA
415 (CRISPR RNA) (50ng/ul), tracrRNA (trans-activating crRNA) (100ng/ul), donor vector
416 (10ng/ul) and TrueCut™ Cas9 Protein v2 (100ng/ul, ThermoFisher) were injected into
417 the pronucleus of one-cell stage zygote from C57BL/6 mice. From 233 zygotes, 57 F0
418 mice were obtained and 3 of them were knockin mice confirmed by PCR, in which the
419 PCR fragments of KI allele with 5'FW and 5'REV primers (1301 bp), and 3'FW and

420 3'REV primers (587 bp) were detected (Supplementary Fig. 4a). The germline
421 transmissions of knockin F0 mice were confirmed by genotyping of F1 mice.

422 **Generation of BM chimeric mice**

423 Recipient B6 mice were lethally irradiated (8.5 Gy, split into 2 doses given 3
424 hours apart) the day before transplantation with 3×10^6 Fscn1-KI BM cells. Mice were
425 used for the experiments at least 8 weeks after transplantation.

426 **In vivo treatment**

427 B16F10 or LLC cells (5×10^5 cells except for Supplementary Fig. 3b: 2×10^5
428 cells) were inoculated subcutaneously (s.c.) into the right flanks of C57BL/6 or Fscn1-KI
429 BMC mice. Anti-PD-L1 mAb (clone 10F.9G2, BioLegend) or Anti-CD4 mAb (clone
430 GK1.5, BioLegend) was injected intraperitoneally (i.p.) at a dose of 200 μg per mouse on
431 days 5 and 9 after tumor inoculation. DT (FUJIFILM Wako) was injected
432 intraperitoneally (i.p.) at a dose of 25 ng/g continuous every second day until day 5.
433 Tumor diameter was measured twice weekly and used to calculate tumor volume (mm^3)
434 [(major axis; mm) x (minor axis; $mm)^2$]. All animal experiments were conducted in
435 accordance with institutional guidelines with the approval of the Animal Care and Use
436 Committee of the Tokyo University of Science.

437 **Tissue collection**

438 Intravascular leukocytes were stained by i.v. injection of FITC-conjugated mAb
439 (3 μg/mouse) against CD45.2 three minutes before sacrifice [47]. Tumors and dLNs (right
440 brachial lymph node) were collected.

441 **Preparing single cell suspension from dLN**

442 dLN cells were prepared by standard method except for Fig. 5, in which dLN
443 was digested for 45 minutes at 37°C with 0.1% collagenase (FUJIFILM Wako) then
444 subjected to 25% Percoll PLUS (Cyvita) gradient and leukocytes were recovered from
445 the pellet. Lineage (CD11b, B220, NK1.1, Ter119) positive cells were depleted using BD
446 IMag Streptavidin Particles Plus-DM (BD Biosciences).

447 The cell concentration of the suspensions was determined using Flow-Count
448 fluorospheres (Beckman Coulter) and a Cytoflex flow cytometer (Beckman Coulter).
449 Cells were then stained with a mix of Fc Block (anti-mouse CD16/CD32 mAb; clone
450 2.4G2, BioLegend) and fluorophore-conjugated anti-mouse mAbs.

451 **Preparing single cell suspension from tumor**

452 Tumors were cut into small fragments and digested for 45 minutes at 37°C with
453 0.1% collagenase (FUJIFILM Wako) in Fig. 1,2,4,5, and 0.1mg/mL Liberase TM (Roche)
454 in Fig. 3. The cells were then subjected to 40% Percoll PLUS (Cytiva) and Histopaque-
455 1083 (Sigma-Aldrich) density separation and leukocytes were recovered from the

456 interphase. The cell concentration of the suspensions was determined using Flow-Count
457 fluorospheres (Beckman) and a Cytoflex flow cytometer (Beckman). Cells were then
458 stained with a mix of Fc Block and fluorophore-conjugated anti-mouse mAbs. TCRβ^+ T
459 cells were enriched magnetically using Anti-APC MicroBeads (Miltenyi) and LS
460 columns (Miltenyi) except for single-cell RNA/TCRseq experiment (Fig. 3). In single-
461 cell RNA/TCRseq experiment, cells were stained with Sample Tag oligonucleotide-
462 conjugated antibodies in Single-Cell Multiplexing Kit (BD Biosciences) as in
463 Supplementary Table S6.

464 **Flow cytometry and cell sorting**

465 CD8$^+$ (Fig. 1, 2, 3, 5), CD8$^+$ PD1$^-$, CD8$^+$ PD1$^+$ Ly108$^+$ Tim3$^-$, CD8$^+$ PD1$^+$
466 Ly108$^+$ Tim3$^+$, and CD8$^+$ PD1$^+$ Ly108$^-$ Tim3$^+$ T cells (Fig. 4) from tumor, and CD8$^+$
467 CD44^{high} T cells from dLN were sorted using FACS Aria II or Aria III (BD Biosciences).
468 Nonviable cells were excluded from the analysis based on forward and side scatter
469 profiles and propidium iodide staining. Intravascular leukocytes were also excluded.
470 Purity of sorted cells was always over 95%. Data were analyzed using FlowJo software
471 (version 10.8.1; BD Biosciences).

472 **TCR library construction and sequencing**

473 <u>For Fig. 1, 2, and 4</u>

474 TCR sequencing libraries for next-generation sequencing were prepared
475 according to the previous report [27]. PolyA RNAs were isolated and amplified from
476 sorted T cells according to a previous report (GSE110711; Shichino et al., 2019). To
477 amplify the TCR cDNA containing complementarity determining region 3 (CDR3),
478 nested PCR of the TCR locus was performed as follows. Beads containing cDNA was
479 resuspended with the 12.5 μL of first PCR mixture comprised 0.5 μL of 10 μM trP1
480 primer, and 1 μL of TCR primer mix (Trac_ex, and Trbc_ex), 4.75 μL of water, and 6.25
481 μL of KAPA Hifi Hotstart ReadyMix (KAPA Biosystems). The thermal cycling
482 conditions were programmed as follows: denaturation at 95°C for 3 minutes, 5 cycles of
483 denaturation for 20 seconds at 98°C, annealing for 15 seconds at 65°C and extension for
484 30 seconds at 72°C, followed by a final extension at 72°C for 2 minutes. Next, 2.5 μL of
485 the first-PCR products were added into the 22.5 μL of second PCR mixture consisted of
486 1.75 μL of 10 μM primer mix (trP1, Trac_in-Bio, and Trbc_in-Bio), 8.25 μL of water
487 and 12.5 μL of KAPA Hifi Hotstart ReadyMix. The thermal cycling conditions were the
488 same as the first PCR except for the cycle number, which was 25 cycles. Next, 25 μL of
489 the second-PCR products were purified using AMPure XP (Beckman-Coulter) at a 0.7:1
490 ratio (beads−to-sample) and eluted in 20 μL of 10mM of Tris HCl pH 8.0.
491 Fragmentasion and adaptor ligation were performed using 10-20ng of second-PCR

492 product as a template with NEBNext Ultra II FS DNA Library Prep Kit for Illumina
493 (New England Biolabs) with some modifications: NEBNext Adaptor for Illumina in
494 "Adaptor Ligation" step was substituted by 5uM P1 Adaptor (duplexed), and the
495 reaction volume was 1/4 of the recommended in all steps. Adaptor-ligated DNA was
496 purified using AM Pure XP kit (Beckman-Coulter) at a 0.8:1 ratio (beads to sample) and
497 eluted in 20 μL of 10mM of Tris HCl pH 8.0. The third PCR was carried out using
498 barcoded primers to enrich the TCRβ cDNA flanked with sequencing adapters. The
499 third PCR mixture consisted of 1 μL of 10 μM trP1 primer, 1 μL of 10 μM IonA-BC[X]-
500 Trbc primer, 3 μL of template and 5 μL of NEBNext Ultra II Q5 Master Mix (accessory
501 of NEBNext Ultra II FS DNA Library Prep Kit). The thermal cycling conditions were
502 programmed as follows: denaturation at 98°C for 30 seconds, 10 cycles of denaturation
503 for 10 seconds at 98°C, annealing and extension for 1minute 15 seconds at 65°C,
504 followed by a final extension at 65°C for 5 minutes. The PCR product was purified and
505 subjected to size selection using AMPure XP kit (Beckman-Coulter) at a 1.0:1 ratio
506 (beads to sample) and eluted with 20 μL of Tris-HCl (pH 8.0). Amplified TCRβ libraries
507 were quantified using a KAPA SYBR Fast qPCR Kit (KAPA Biosystems) and size
508 distribution was analyzed by Microchip Electrophoresis System MultiNA (Shimadzu).
509 Final TCRβ libraries, whose lengths were 200–300 base pairs, were pooled and

510 sequenced using an Ion 540 Kit Chef, an Ion 540 Chip kit, and an Ion Genestudio S5

511 Sequencer (Thermo Fisher Scientific) according to the manufacturer's instructions,

512 except the flow number (500).

513 For Fig. 5

514 TCR sequencing libraries for next-generation sequencing were prepared

515 according to the previous report [44]. In brief, mRNA in T-cell lysate was captured by 10

516 μL of Dynabeads M270 streptavidin (Thermo Fisher Scientific) bound to 2.5 pmol of

517 BioEcoP-dT25-adapter primers. To perform reverse transcription and template-

518 switching, mRNA-trapped beads were suspended in 10 μL of RT mix [1× First Strand

519 buffer (Thermo Fisher Scientific), 1 mM dNTP (Roche), 2.5 mM DTT (Thermo Fisher

520 Scientific), 1 M betaine (Sigma-Aldrich), 9 mM MgCl2 (NIPPON GENE), 1 U/μL

521 RNaseIn Plus RNase Inhibitor (Promega), 10 U/μL Superscript II (Thermo Fisher

522 Scientific), and 1 μM of i5-TSO], and incubated for 60 min at 42ºC and immediately

523 cooled on ice. To amplify the TCR cDNA containing complementarity determining

524 region 3 (CDR3), nested PCR of the TCR locus was performed following the

525 purification of PCR product by an AM Pure XP kit (Beckman Coulter) at a 0.7:1 ratio of

526 beads to sample and eluted with 20 μL of 10 mM Tris-HCl (pH 8.0). To amplify TCR

527 libraries and add adaptor sequences for the next-generation sequencer, the third PCR

528 was performed. The third-PCR products were purified as second PCR. The products
529 were pooled and then purified and subjected to dual size selection using ProNex size-
530 selective purification system (Promega) and eluted with 25 μL of 10 mM Tris-HCl (pH
531 8.5). Final TCR libraries, whose lengths were about 600 base pairs were sequenced
532 using an Illumina Novaseq 6000 S4 flowcell (67 bp read 1 and 140 bp read 2)
533 (Illumina). Only read2 contained the sequence regarding the definition of T cell clones.

534 **Library preparation and sequencing for scRNA/TCRseq**

535 T cells from the spleen of Pmel Tg mouse, which stained with Single-Cell
536 Multiplexing Kit (BD Biosciences) as in Supplementary Table S6, were spiked in after
537 cell sorting. Live cells were stained with Calcein AM (Nacalai) and counted using
538 Flow-Count fluorospheres (Beckman) and a Cytoflex flow cytometer (Beckman). About
539 18,000 labeled cells were trapped and reverse-transcribed using the BD Rhapsody™
540 (BD), Targeted mRNA and AbSeq Amplification Kit (BD), and Immune Response Panel
541 Mm (BD) according to the manufacturer's instructions. Targeted mRNA, TCRseq and
542 Sample Tag libraries were prepared using according to the manufacturer's instructions
543 (VDJ CDR3 and Sample Tag Library Preparation Protocol) with the following
544 modifications; (1) BD Rhapsody™ Immune Response Panel Mm with supplement panel
545 including Cmpk2, Ifi204, Ifi211, Ifit1, Ifit3, Ifit3b, Ifit3b, Isg15, Mx1, Rsad2, and

546 Usp18 were used for target mRNA amplification. (2) we used original set of primer for
547 TCR amplification as summarized in Key resources table, and performed additional
548 PCR (3rd PCR, 6 cycles) to introduce unique dual index for sequencing. (3) we used
549 ProNex Size-Selection DNA purification System (Promega) for purification of PCR
550 product. Primers used for each PCR reaction and sample-to-beads ratios for purifying
551 PCR product were summarized in Supplementary Table S7. Amplified libraries were
552 quantified using a KAPA SYBR Fast qPCR Kit (KAPA Biosystems) and size
553 distribution was analyzed by Microchip Electrophoresis System MultiNA (Shimadzu).
554 Targeted RNAseq and Sample Tag libraries were sequenced on an Illumina Novaseq
555 6000 S4 flowcell (67 bp read 1 and 140 bp read 2) (Illumina) to a depth of
556 approximately 40,000 reads and 10,000 reads per cell, respectively. TCRseq libraries
557 were sequenced on an Illumina Novaseq 6000 SP flowcell (67 bp read 1 and 459 bp
558 read 2) (Illumina) to a depth of approximately 20,000 reads.

559 **Data processing of TCR sequencing**

560 Adapter trimming and quality filtering of sequencing data were performed by
561 using Cutadapt-3.2 (Martin, 2013) and PRINSEQ-0.20.4 [50]. Sequencing data were
562 processed by MiXCR-3.0.5 [51]. In MiXCR, filtered reads were aligned to reference
563 mouse TCR V/D/J sequences registered in the international ImMunoGeneTics (IMGT)

564 information system: -vParameters.geneFeatureToAlign = VTranscript -

565 vjAlignmentOrder = JThenV, then identical sequences were assembled and grouped in

566 clones with PCR and sequencing error correlation with the following parameters: -

567 badQualityThreshold=10, –separateByV=true, --only-productive=true, –region-of-

568 interest=CDR3. The Variable (V) and Joining (J) segment of TCRs were represented in

569 IMGT gene nomenclature.

570 List of final clones were analyzed by VDJtools-1.2.1 [52]. Then, the sequencing

571 reads of sample was normalized to the cell count in each sample by "DownSample"

572 command of VDJtools. T-cell clones were determined as TCR reads with the same TCR

573 V segment, J segment and CDR3 nucleotide sequence.

574 **Calculation of clonality of TCR repertoire**

575 The 1 - Pielou index was used to evaluate the clonality of TCR repertoire, which

576 was calculated using the formula $1 - \sum_{i=1}^{n} p_i \log_e(p_i) / \log_e(n)$, where p_i is the

577 frequency of clone *i* for a sample with *n* unique clones.

578 **Identification of OL clones in oligoclonal and polyclonal fraction**

579 dLN-tumor OL clones were identified by "JoinSamples" function in VDJtools.

580 These OL clones were ranked in order of their frequency in the tumor. OL clones that

581 ranked in top 10 were defined as oligoclonal fraction of OL repertoire, and the other OL

582 clones were defined as polyclonal fraction. In the scRNA/TCRseq analysis, OL clones
583 were defined as those whose TCRb sequence (V segment, J segment and CDR3
584 nucleotide) was identified in the repertoire of dLN $CD8^{+}$ $CD44^{high}$ T cells, the output of
585 bulk TCRseq. The oligoclonal/polyclona fraction in scTCR analysis on TILs was defined
586 based on the frequency calculated in scTCRseq analysis.

587 **Data processing of scRNAseq reads**

588 Data processing of scRNAseq reads was performed as described in Shichino et
589 al. (TAS-seq). Adapter trimming of sequencing data was performed using cutadapt 2.10
590 (Martin, 2013). Filtered cell barcode reads were annotated by Python script provided by
591 BD Biosciences with minor modification for compatibility to Python 3.7. Associated
592 cDNA reads were mapped to reference RNA using bowtie2-2.4.2 [53] by the following
593 parameters: -p 2 --very-sensitive-local -N 1 -norc -seed 656565 -reorder. Then, cell
594 barcode information of each read was added to the bowtie2-mapped BAM files by the
595 python script and pysam 0.15.4 [54], and read counts of each gene in each cell barcode were
596 counted using mawk. Resultant count data was converted to a single-cell gene-expression
597 matrix file by using R-3.6.3. The inflection point of the knee-plot (total read count versus
598 the rank of the read count) was detected using DropletUtils package (v1.14.1, Lun *et al.*,
599 2018) in R-3.6.3. Cells of which total read count was over inflection point were

600 considered as valid cells.

601 **Data processing of sample tag reads**

602 For sample tag data, adapter trimming of sequencing data was performed by
603 using cutadapt 3.4 (Martin, 2013). Filtered reads were chunked to 64 parts for parallel
604 processing by using Seqkit 0.15.0 [56]. Filtered cell barcode reads were annotated by Python
605 script provided by BD with minor modification for compatible to Python3.8. Associated
606 sample tag reads were mapped to known barcode fasta by using bowtie2-2.4.2 [53] by the
607 following parameters: -p 2 -D 50 -R 20 -N 0 -L 14 -i S,1,0.75 –norc –seed 656565 –
608 reorder –trim-to 3:40 –score-min L,-9,0 –mp 3,3 –np 3 –rdg 3,3.

609 Then, cell barcode information of each read were added to the bowtie2-mapped
610 BAM files, and read counts of each Tag in each cell barcode were counted by using
611 mawk. Resulted count data was converted to Tags x cells matrix file by using data.table
612 package in R 3.6.3, and top 1M cell barcodes were extracted. For assignment of each
613 tags to each cell barcodes, read counts of each tag in each valid cell barcode, which
614 defined by the cDNA matrix, were extracted from tag/cell barcode expression matrix.
615 Unassigned cell barcodes were labeled as “not-detected” cells. Then, sum of the total
616 read counts of each tags were normalized to the minimum sum count of each tags, and
617 $\log_2$ fold-change between first most tag counts and second most tag counts within each

618 cell barcode. Each cell barcode was ranked by the fold-change ascending order, and top
619 N cells were identified as doublets (N was calculated as theoretically detectable
620 doublets calculated by the Poisson's distribution based on the number of loaded cells,
621 total Rhapsody well number, and number of tags used).

622 **scRNAseq data analysis**

623 scRNAseq data analysis was performed by using the R software package Seurat
624 v4.0.1 [57]. Expression data of targeted panel genes were converted to the Seurat object.
625 Then, genes not included in the target panel and doublet or spiked-in Pmel cells were
626 excluded. Expression data was log normalized and scaled using NormalizeData and
627 ScaleData function, respectively. Principal component analysis (PCA) against all genes
628 included in target panel was performed using RunPCA (number of calculated principal
629 components (PCs) were 100), and enrichment of each PC was calculated using the
630 JackStraw and ScoreJackStraw function (num.replicate = 100), and PCs that were
631 significantly enriched ($p \leq 0.05$) were selected for clustering and dimensional reduction
632 analysis. Dimensional reduction was performed using RunUMAP. Cell clustering was
633 performed using FindNeighbors and FindClusters against the significant PCs. Marker
634 genes of each identified cluster were identified using FindAllMarkers function
635 (test.use="wilcox", min.pct=0.1, return.thresh=0.05). Cluster constituted with

636 contaminant cells determined by marker genes were excluded and the above analysis
637 procedure was repeated.

638 **Transcriptional signature analysis in scRNAseq**

639 We computed the extent to which gene signatures were expressed in cells using
640 Seurat's "AddModuleScore" function. Progenitor and terminally exhausted signature
641 genes were obtained from the dataset of Miller et al. [29]. Cytotoxicity and proliferation
642 signature genes were selected according to the descriptions in BD Rhapsody™ Immune
643 Response Panel Mm (BD). Genes used for calculating signature scores were summarized
644 in Supplementary Table S8.

645 **Pseudotime analysis on scRNAseq data**

646 Pseudotime analysis was performed using the Bioconductor package Slingshot
647 v2.2.0 (Street et al., 2018). We ran the analysis using significantly enriched PCs ($p \leq 0.05$)
648 after setting Cluster 7 (NV-like) as the start cluster.

649 **Data processing of scTCRseq**

650 Raw data of single-cell TCR sequencing were processed by pipeline produced
651 by ImmunoGeneTeqs, Inc.. Briefly, sequencing reads were first separated by cell barcode,
652 then adapter trimming and quality filtering of sequencing data were performed by using
653 Cutadapt (Martin, 2013). PCR and sequencing error were corrected by lighter v1.1.2 [59]

654 with following parameters: -newQual 25 -maxcor 4 -K 20. Error-corrected sequence reads
655 were processed by MiXCR [51] to generate the list of TCRα or TCRβ sequences for each
656 cell barcode, using reference mouse TCR V/D/J sequences registered in the international
657 IMGT information system with the parameters summarized in Supplementary Table S9.
658 Quality filtering of cell barcodes was performed with the following criteria: (1) more than
659 32 TCR reads were detected. (2) the proportion of the most frequent TCR sequence in
660 cell barcode was over 0.6. (3) the cell barcode was annotated to the T cell cluster in
661 scRNAseq analysis. Finally, the most frequent sequence of TCRα and TCRβ was adopted
662 and paired in each cell barcode. Identified TCRα/β sequence was imported into the
663 meta.data matrix in Seurat object of scRNAseq data based on the cellular barcode
664 identities. T-cell clones were determined as cells with the same TCRα and TCRβ pair,
665 defined by V segment, J segment and CDR3 nucleotide sequence. Frequency of each
666 clone was calculated as the proportion of cells belonging to the clone in all T cells whose
667 TCRα and TCRβ pair was assigned.

668 **Evaluating the exhaustion status of T cell clones by TCRseq on CD8$^+$ TIL subsets.**

669 To evaluate the exhaustion status of OL clones in oligoclonal and polyclonal
670 fraction, we first calculated the frequency of clones in "Pooled" CD8$^+$ TIL repertoire from
671 the repertoire of TIL subsets (PD1$^-$, Ly108, DP, and Tim-3) as the following equation:

672 $$Freq_{k\ Pooled} = \frac{\sum_i Freq_{k\ i} \times Count_i}{\sum_i Count_i},$$

673 where *Freq* means the frequency of each clone k, and *Count* means the cell count of each

674 subset i. Then, OL clones in oligoclonal and polyclonal fraction was identified based on

675 their frequency in Pooled repertoire as above. The total frequency of these clones in each

676 TIL subset was calculated, and defined as oligoclonal and polyclonal OL repertoire in

677 each TIL subset.

678 **Quantification and statistical analysis**

679 Statistical analyses were performed using GraphPad Prism (ver9.2.0) software

680 (GraphPad Software) except for correlation analysis in Fig. 2e and 3g. One-way ANOVA

681 with Tukey's post test was run on the comparison between treatment groups. Spearman

682 correlation test was run on the correlation analysis using cor.test function in Microsoft R

683 open 4.1.1. One-way Repeated-Measures (RM) ANOVA with Tukey's post test was run

684 on the comparison between $CD8^+$ TIL subsets. Paired t test was run on the comparison

685 between the dominance of oligoclonal or polyclonal fraction of dLN-tumor OL. Multiple

686 unpaired t tests was run on the comparison between DT treated and untreated mice for

687 each treatment group. Asterisks to indicate significance corresponding to the following:

688 n.s., not significant (P>0.05), *$P \leq 0.05$, **$P \leq 0.01$, *** $P \leq 0.001$.

689

690 **Acknowledgements**

691 We would like to thank Y. Hara for advice in cell sorting, staff of RIBS animal
692 facility for supporting the maintenance of animals, member of IGT. Inc. for expert
693 technical assistance in TCR sequencing, D. Komura and S. Ishikawa for advice in data
694 analysis. We would also like to thank Editage (www.editage.com) for English language
695 editing. Fig. 5a was created with BioRender.com.

696 This work was supported by the Japan Society for the Promotion of Science
697 under Grant Number 20281832 and 17929397, and by the Japan Agency for Medical
698 Research and Development (AMED) under Grant Number JP 21gm6210025,
699 22fk0310509s0101, and 22ama221306h0001.

700

701 **Author Contributions**

702 H.A., K.M., and S.U. designed research. H.A. and S.U. performed research. T.A.
703 generated mice. H.A., M.T., H.O., H.S., H.A., and S.U. processed the samples. H.A.
704 analyzed data with supports from S.S. and S.U.. H.A. and S.U. wrote the initial draft of
705 the manuscript. All the authors participated in writing the final manuscript.

706

707 **Competing Interests statement**

708 H.A. reports stock for ImmunoGeneTeqs, Inc. S.U. reports advisory role for
709 ImmunoGeneTeqs, Inc; stock for ImmunoGeneTeqs, Inc, IDAC Theranostics, Inc. S.S.
710 reports advisory role for ImmunoGeneTeqs, Inc; stock for ImmunoGeneTeqs, Inc, K.M.
711 reports consulting or advisory role for Kyowa-Hakko Kirin, ImmunoGeneTeqs, Inc;
712 research funding from Kyowa-Hakko Kirin, and Ono; stock for ImmunoGeneTeqs, Inc,
713 IDAC Theranostics, Inc.

714

715 **References**

716 1. Ribas, A. & Wolchok, J. D. Cancer immunotherapy using checkpoint blockade.
717 *Science (80-.).* **359**, 1350–1355 (2018).
718 2. Havel, J. J., Chowell, D. & Chan, T. A. The evolving landscape of biomarkers for
719 checkpoint inhibitor immunotherapy. *Nat. Rev. Cancer* **19**, 133–150 (2019).
720 3. Pasetto, A. *et al.* Tumor- and Neoantigen-Reactive T-cell Receptors Can Be
721 Identified Based on Their Frequency in Fresh Tumor. *Cancer Immunol. Res.* **4**,
722 734–743 (2016).
723 4. Gros, A. *et al.* PD-1 identifies the patient-specific CD8+ tumor-reactive
724 repertoire infiltrating human tumors. *Journal of Clinical Investigation* **124**, 2246–
725 2259 (2014).

726 5. Oliveira, G. *et al.* Phenotype, specificity and avidity of antitumour CD8+ T cells
727 in melanoma. *Nature* **596**, 119–125 (2021).
728 6. Overwijk, W. W. *et al.* Tumor regression and autoimmunity after reversal of a
729 functionally tolerant state of self-reactive CD8+ T cells. *J. Exp. Med.* **198**, 569–
730 580 (2003).
731 7. Ahmadzadeh, M. *et al.* Tumor antigen-specific CD8 T cells infiltrating the tumor
732 express high levels of PD-1 and are functionally impaired. *Blood* **114**, 1537–1544
733 (2009).
734 8. Aversa, I., Malanga, D., Fiume, G. & Palmieri, C. Molecular T-cell repertoire
735 analysis as source of prognostic and predictive biomarkers for checkpoint
736 blockade immunotherapy. *Int. J. Mol. Sci.* **21**, (2020).
737 9. Kidman, J. *et al.* Characteristics of TCR Repertoire Associated With Successful
738 Immune Checkpoint Therapy Responses. *Front. Immunol.* **11**, 1–11 (2020).
739 10. Zhang, J. *et al.* Compartmental analysis of T-Cell clonal dynamics as a function
740 of pathologic response to neoadjuvant PD-1 blockade in resectable non-small cell
741 lung cancer. *Clin. Cancer Res.* **26**, 1327–1337 (2020).
742 11. Casarrubios, M. *et al.* Pretreatment Tissue TCR Repertoire Evenness Is
743 Associated with Complete Pathologic Response in Patients with NSCLC

744 Receiving Neoadjuvant Chemoimmunotherapy. *Clin. Cancer Res.* (2021).
745 doi:10.1158/1078-0432.ccr-21-1200
746 12. Chiffelle, J. *et al.* T-cell repertoire analysis and metrics of diversity and clonality.
747 *Curr. Opin. Biotechnol.* **65**, 284–295 (2020).
748 13. Yusko, E. *et al.* Association of Tumor Microenvironment T-cell Repertoire and
749 Mutational Load with Clinical Outcome after Sequential Checkpoint Blockade in
750 Melanoma. *Cancer Immunol. Res.* **7**, 458–465 (2019).
751 14. Riaz, N. *et al.* Tumor and Microenvironment Evolution during Immunotherapy
752 with Nivolumab. *Cell* **171**, 934-949.e15 (2017).
753 15. Dovedi, S. J. *et al.* Fractionated radiation therapy stimulates antitumor immunity
754 mediated by both resident and infiltrating polyclonal T-cell populations when
755 combined with PD-1 blockade. *Clin. Cancer Res.* **23**, 5514–5526 (2017).
756 16. Li, H. *et al.* Dysfunctional CD8 T Cells Form a Proliferative, Dynamically
757 Regulated Compartment within Human Melanoma. *Cell* **176**, 775-789.e18
758 (2019).
759 17. van der Leun, A. M., Thommen, D. S. & Schumacher, T. N. CD8+ T cell states
760 in human cancer: insights from single-cell analysis. *Nat. Rev. Cancer* **20**, 218–
761 232 (2020).

762 18. McLane, L. M., Abdel-Hakeem, M. S. & Wherry, E. J. CD8 T Cell Exhaustion
763 During Chronic Viral Infection and Cancer. *Annu. Rev. Immunol.* **37**, 457–495
764 (2019).
765 19. Gueguen, P. *et al.* Contribution of resident and circulating precursors to tumor-
766 infiltrating CD8+ T cell populations in lung cancer. *Sci. Immunol.* **6**, (2021).
767 20. Simoni, Y. *et al.* Bystander CD8+ T cells are abundant and phenotypically
768 distinct in human tumour infiltrates. *Nature* **557**, 575–579 (2018).
769 21. Chen, D. S. & Mellman, I. Oncology meets immunology: The cancer-immunity
770 cycle. *Immunity* **39**, 1–10 (2013).
771 22. Aoki, H., Shichino, S., Matsushima, K. & Ueha, S. Revealing Clonal Responses
772 of Tumor-Reactive T-Cells Through T Cell Receptor Repertoire Analysis. *Front.*
773 *Immunol.* **13**, 1–10 (2022).
774 23. Yost, K. E. *et al.* Clonal replacement of tumor-specific T cells following PD-1
775 blockade. *Nat. Med.* **25**, 1251–1259 (2019).
776 24. Ueha, S. *et al.* Robust Antitumor Effects of Combined Anti-CD4-Depleting
777 Antibody and Anti-PD-1/PD-L1 Immune Checkpoint Antibody Treatment in
778 Mice. *Cancer Immunol. Res.* **3**, 631–640 (2015).
779 25. Aoki, H. *et al.* TCR repertoire analysis reveals mobilization of novel CD8 + T

780 cell clones into the cancer-immunity cycle following anti-CD4 antibody
781 administration. *Front. Immunol.* **10**, 1–13 (2019).
782 26. Shitara, K. *et al.* First-in-human phase 1 study of IT1208, a defucosylated
783 humanized anti-CD4 depleting antibody, in patients with advanced solid tumors.
784 *J. Immunother. Cancer* **7**, 1–11 (2019).
785 27. Aoki, H. *et al.* Transient depletion of CD4þ cells induces remodeling of the TCR
786 repertoire in gastrointestinal cancer. *Cancer Immunol. Res.* **9**, 624–636 (2021).
787 28. Thommen, D. S. *et al.* A transcriptionally and functionally distinct pd-1 + cd8 + t
788 cell pool with predictive potential in non-small-cell lung cancer treated with pd-1
789 blockade. *Nat. Med.* **24**, (2018).
790 29. Miller, B. C. *et al.* Subsets of exhausted CD8+ T cells differentially mediate
791 tumor control and respond to checkpoint blockade. *Nat. Immunol.* **20**, 326–336
792 (2019).
793 30. Siddiqui, I. *et al.* Intratumoral Tcf1 + PD-1 + CD8 + T Cells with Stem-like
794 Properties Promote Tumor Control in Response to Vaccination and Checkpoint
795 Blockade Immunotherapy. *Immunity* **50**, 195-211.e10 (2019).
796 31. Kallies, A., Zehn, D. & Utzschneider, D. T. Precursor exhausted T cells: key to
797 successful immunotherapy? *Nat. Rev. Immunol.* **20**, 128–136 (2020).

798 32. Salmon, H. *et al.* Expansion and Activation of CD103+ Dendritic Cell
799 Progenitors at the Tumor Site Enhances Tumor Responses to Therapeutic PD-L1
800 and BRAF Inhibition. *Immunity* **44**, 924–938 (2016).
801 33. Roberts, E. W. *et al.* Critical Role for CD103+/CD141+ Dendritic Cells Bearing
802 CCR7 for Tumor Antigen Trafficking and Priming of T Cell Immunity in
803 Melanoma. *Cancer Cell* **30**, 324–336 (2016).
804 34. Qureshi, O. S. *et al.* Trans-endocytosis of CD80 and CD86: A molecular basis for
805 the cell-extrinsic function of CTLA-4. *Science (80-.).* **332**, 600–603 (2011).
806 35. Lamb, M. C. & Tootle, T. L. Fascin in cell migration: More than an actin
807 bundling protein. *Biology (Basel).* **9**, 1–18 (2020).
808 36. Adams, J. C. Roles of fascin in cell adhesion and motility. *Curr. Opin. Cell Biol.*
809 **16**, 590–596 (2004).
810 37. Yamakita, Y. *et al.* Fascin1 Promotes Cell Migration of Mature Dendritic Cells.
811 *J. Immunol.* **186**, 2850–2859 (2011).
812 38. Zhang, F. R. *et al.* Fascin expression in human embryonic, fetal, and normal adult
813 tissue. *J. Histochem. Cytochem.* **56**, 193–199 (2008).
814 39. Rudqvist, N. P. *et al.* Radiotherapy and CTLA-4 blockade shape the tcr repertoire
815 of tumor-infiltrating t cells. *Cancer Immunol. Res.* **6**, 139–150 (2018).

816 40. Clarke, J. *et al.* Single-cell transcriptomic analysis of tissue-resident memory T
817 cells in human lung cancer. *J. Exp. Med.* **216**, 2128–2149 (2019).
818 41. Zhang, L. *et al.* Lineage tracking reveals dynamic relationships of T cells in
819 colorectal cancer. *Nature* **564**, 268–272 (2018).
820 42. Dammeijer, F. *et al.* The PD-1/PD-L1-Checkpoint Restrains T cell Immunity in
821 Tumor-Draining Lymph Nodes. *Cancer Cell* **38**, 685-700.e8 (2020).
822 43. Zemek, R. M. *et al.* Bilateral murine tumor models for characterizing the
823 response to immune checkpoint blockade. *Nat. Protoc.* **15**, 1628–1648 (2020).
824 44. Tsunoda, M. *et al.* Proportional Tumor Infiltration of T Cells via Circulation
825 Duplicates the T Cell Receptor Repertoire in a Bilateral Tumor Mouse Model.
826 *Front. Immunol.* **12**, 1–12 (2021).
827 45. Memarnejadian, A. *et al.* PD-1 Blockade Promotes Epitope Spreading in
828 Anticancer CD8 + T Cell Responses by Preventing Fratricidal Death of
829 Subdominant Clones To Relieve Immunodomination . *J. Immunol.* **199**, 3348–
830 3359 (2017).
831 46. Abe, T., Inoue, K. ichi, Furuta, Y. & Kiyonari, H. Pronuclear Microinjection
832 during S-Phase Increases the Efficiency of CRISPR-Cas9-Assisted Knockin of
833 Large DNA Donors in Mouse Zygotes. *Cell Rep.* **31**, 107653 (2020).

834 47. Anderson, K. G. *et al*. Intravascular staining for discrimination of vascular and
835 tissue leukocytes. *Nat Protoc.* **9**, 209-222 (2014).
836 48. Shichino, S. *et al.* Transcriptome network analysis identifies protective role of
837 the LXR/SREBP-1c axis in murine pulmonary fibrosis. *JCI Insight* **4**, (2019).
838 49. Martin, M. Cutadapt removes adapter sequences from high-throughput
839 sequencing reads. *EMBnet.journal* **17**, 10–12 (2013).
840 50. Schmieder, R. & Edwards, R. Quality control and preprocessing of metagenomic
841 datasets. *Bioinformatics* **27**, 863–864 (2011).
842 51. Bolotin, D. A. *et al.* MiXCR: Software for comprehensive adaptive immunity
843 profiling. *Nat. Methods* **12**, 380–381 (2015).
844 52. Shugay, M. *et al.* VDJtools: Unifying Post-analysis of T Cell Receptor
845 Repertoires. *PLoS Comput. Biol.* **11**, 1–16 (2015).
846 53. Langmead, B. & Salzberg, S. L. Fast gapped-read alignment with Bowtie 2. *Nat.*
847 *Methods* **9**, 357–359 (2012).
848 54. Li, H. *et al.* The Sequence Alignment/Map format and SAMtools. *Bioinformatics*
849 **25**, 2078–2079 (2009).
850 55. Lun, A. T. L. *et al.* EmptyDrops: distinguishing cells from empty droplets in
851 droplet-based single-cell RNA sequencing data. *Genome Biol* **20**, 63 (2019).

852 doi:10.1101/234872

853 56. Shen, W., Le, S., Li, Y. & Hu, F. SeqKit: A cross-platform and ultrafast toolkit

854 for FASTA/Q file manipulation. *PLoS One* **11**, 1–10 (2016).

855 57. Hao, Y. *et al.* Integrated analysis of multimodal single-cell data. *Cell* **184**, 3573-

856 3587.e29 (2021).

857 58. Street, K. *et al.* Slingshot: cell lineage and pseudotime inference for single-cell

858 transcriptomics. *BMC Genomics* **19**, 477 (2018).

859 59. Song, L., Florea, L. & Langmead, B. Lighter: fast and memory-efficient

860 sequencing error correction without counting. *Genome Biol.* **15**, 509 (2014).

861

862 **Figure legends**

863 **Fig. 1 The dLN-tumor repertoire overlap increases following anti-PD-L1 and anti-**

864 **CD4 treatments. a.** Experimental procedure. **b**, **c.** Growth curve (**b**) and weight (**c**) of

865 the tumor. **d, e.** Gating strategy for sorting the $CD8^+$ $CD44^{high}$ T cells in the dLN (**d**) and

866 the $CD8^+$ T cells in the tumor (**e**). **f.** Scheme of the dLN-tumor repertoire overlap analysis.

867 **g.** Representative plot of the dLN-tumor repertoire overlap for each treatment group. The

868 plot exhibits the top 20 OL clones (colored), the OL clones other than the top 20 ones

869 (dark gray), and the non-OL clones (gray). **h, i.** Frequency of the OL clones in the dLN

870 (**h**) and the tumor (**i**).

871 Means ± SEM are shown (n = 6–10 per group). One-way ANOVA and Tukey's *post-hoc*

872 test were used in (**b**), (**c**), (**h**), and (**i**); *$P \leq 0.05$; ** $P \leq 0.01$; *** $P \leq 0.001$.

873

874 **Fig. 2 Increase in the polyclonal fraction of the dLN-tumor OL repertoire following**

875 **anti-PD-L1 and anti-CD4 treatments. a, b.** Flow chart (**a**) and representative plot (**b**)

876 used for defining the oligoclonal and polyclonal fractions of the dLN-tumor OL repertoire.

877 In (**b**), the frequency of individual clones is plotted according to their rank in the tumor

878 in descending order. The top 10 (oligoclonal fraction) and 11th or lower (polyclonal

879 fraction) OL clones are colored in red and blue, respectively. **c, d.** Total frequency of the

880 oligoclonal and polyclonal fractions of the OL clones in the tumor. **e.** Correlation between

881 the tumor volume and the total frequency of the oligoclonal (left) or polyclonal (right)

882 fraction of OL clones in the tumor.

883 Means are shown (n = 6–10 per group) (**c**); means ± SEM are shown (n = 6–10 per group).

884 One-way ANOVA and Tukey's *post-hoc* test were used in (**d**); Spearman correlation test

885 was used in (**e**); *$P \leq 0.05$; *** $P \leq 0.001$.

886

887 **Fig. 3 Single-cell analysis of the dLN-tumor OL clones following anti-CD4 mAb**

888 **treatment. a.** Experimental procedure. **b.** Uniform manifold approximation and
889 projection (UMAP) plot of the scRNA-seq data of $CD8^+$ TILs following anti-CD4
890 treatment. **c.** Violin plot showing the expression of marker genes in the T-cell subsets. **d.**
891 Violin plot showing the module scores of the feature genes of progenitor (top) and
892 terminally (bottom) exhausted T cells. **e.** UMAP showing the T cells in the oligoclonal or
893 polyclonal fraction of the dLN-tumor OL repertoire (left). Pie chart showing the
894 proportion of T cells in the "naïve-like" (pink) or "progenitor exhausted" (purple) clusters
895 in the oligoclonal or polyclonal fraction (right). **f.** Bar chart showing the proportion of the
896 oligoclonal (red) and polyclonal (blue) fractions of the OL clones and the non-OL clones
897 (gray) in each cluster. **g.** Correlation between the clone's frequency in the tumor and the
898 progenitor or terminally exhausted score of each clone. The progenitor or terminally
899 exhausted score was calculated for each cell as in (**d**), and the average value was then
900 calculated for each clone.
901 Pearson correlation test was used in (**e**); Tex: terminally exhausted; Tex int: intermediately
902 exhausted; Tex prog: progenitor exhausted; IFN resp.: IFN responding; NV-like: naïve-
903 like; Prolif.: proliferating.
904
905 **Fig. 4 Oligoclonal and polyclonal fractions of the dLN-tumor OL repertoire in $CD8^+$**

906 **TIL subsets following anti-CD4 mAb treatment. a.** Gating strategy used for sorting the

907 PD1$^-$, Ly108, DP, and Tim-3 CD8$^+$ TIL subsets in anti-CD4 treated mice. **b.** Clonality of

908 the CD8$^+$ TIL subsets. **c.** Example of the estimation of clone frequency in pooled CD8$^+$

909 TILs based on the frequencies in each CD8$^+$ TIL subset. **d.** Frequency of the oligoclonal

910 (red) or polyclonal (blue) fraction of OL clones in the CD8$^+$ TIL subsets. Lines indicate

911 the data from the same mice. **e.** Bar chart showing the proportion of the oligoclonal (red)

912 or polyclonal (blue) fraction of the OL clones in each CD8$^+$ TIL subset.

913 Mean ± SEM is shown in (**b**) and the mean is shown in (**e**) (n = 5 per group) (**b**); one-way

914 RM ANOVA and Tukey's *post-hoc* test were used in (**b**) and (**d**); paired t-test was used

915 in (E); *$P \leq 0.05$; ** $P \leq 0.01$.

916

917 **Fig. 5 Decrease in the polyclonal fraction of the dLN-tumor OL repertoire by**

918 **depleting migratory DCs following anti-PD-L1 and anti-CD4 treatments. a.**

919 Experimental procedure. **b, c.** Representative flow cytometry plot of the dLN lineage$^-$

920 cells for CCR7$^+$ CD11c^{int} (**b**) and CCR7$^+$ DTR$^+$ (**c**) migratory DCs (migDCs) in untreated

921 or DT-treated mice on day 14. **d.** Comparison of the frequency of CCR7$^+$ CD11c^{int}

922 migDCs in dLN between DT-treated and untreated mice. **e.** Comparison of the frequency

923 of OL clones in the tumor between DT-treated and untreated mice. **f, g.** Comparison of

924 the frequency of the oligoclonal (F) and polyclonal (G) fraction of dLN-tumor OL clones

925 in the tumor between DT-treated and untreated mice.

926 **a.** was created using BioRender.com; means ± SEM are shown (n = 4–5 per group);

927 multiple unpaired t-tests were used in (**d**), (**e**), (**f**) and (**g**); *$P \leq 0.05$; ** $P \leq 0.01$; *** P

928 ≤ 0.001.

Figure 1

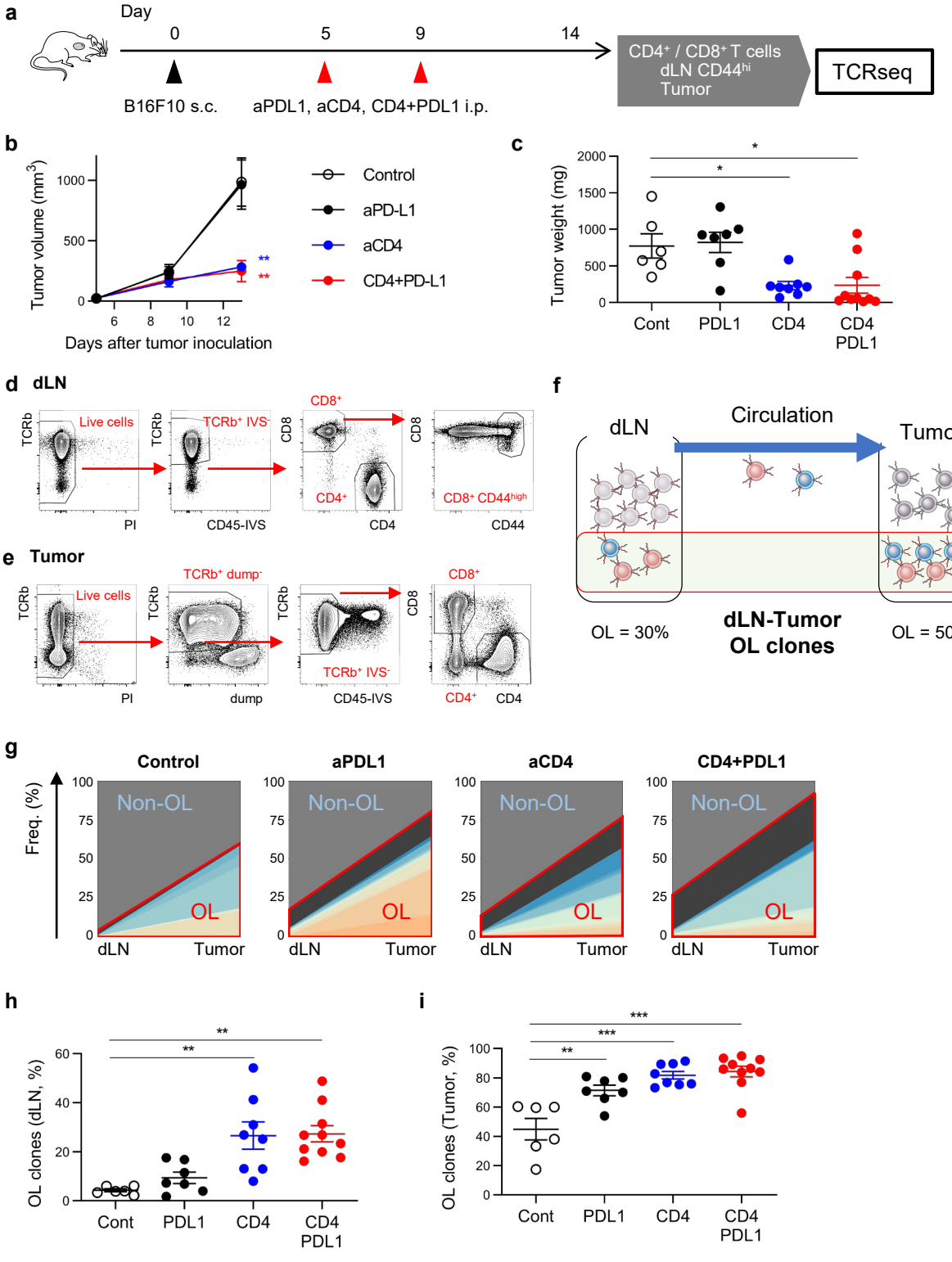
a
Day
0
5
9
14
B16F10 s.c.
aPDL1, aCD4, CD4+PDL1 i.p.
CD4+ / CD8+ T cells
dLN CD44hi
Tumor
TCRseq
b
Tumor volume (mm3)
Days after tumor inoculation
Control
aPD-L1
aCD4
CD4+PD-L1
c
Tumor weight (mg)
Cont
PDL1
CD4
CD4 PDL1
d dLN
Live cells
TCRb+ IVS-
CD8+
CD4+
CD8+ CD44high
PI
CD45-IVS
CD4
CD44
e Tumor
Live cells
TCRb+ dump-
TCRb+ IVS-
CD8+
CD4+
PI
dump
CD45-IVS
CD4
f
dLN
Circulation
Tumor
OL = 30%
dLN-Tumor
OL clones
OL = 50%
g
Control
aPDL1
aCD4
CD4+PDL1
Freq. (%)
Non-OL
OL
dLN
Tumor
h
OL clones (dLN, %)
Cont
PDL1
CD4
CD4 PDL1
i
OL clones (Tumor, %)
Cont
PDL1
CD4
CD4 PDL1

Figure 2

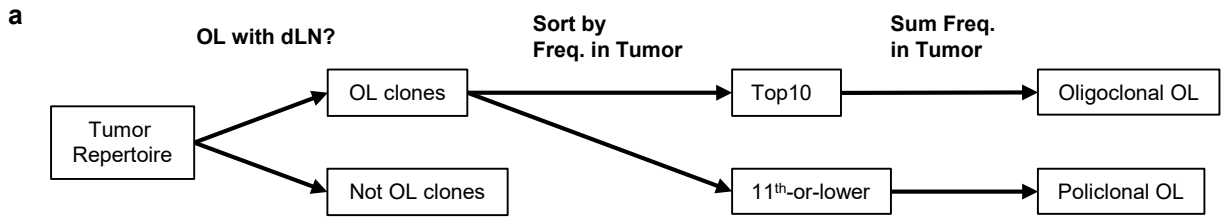
a
OL with dLN?
Sort by
Freq. in Tumor
Sum Freq.
in Tumor
Tumor
Repertoire
OL clones
Not OL clones
Top10
11th-or-lower
Oligoclonal OL
Policlonal OL

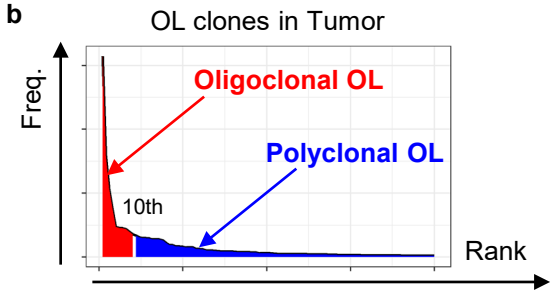
b
OL clones in Tumor
Freq.
Oligoclonal OL
Polyclonal OL
10th
Rank

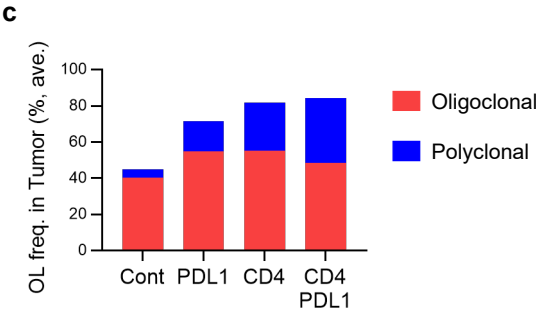
c
OL freq. in Tumor (%, ave.)
100
80
60
40
20
0
Cont
PDL1
CD4
CD4
PDL1
Oligoclonal
Polyclonal

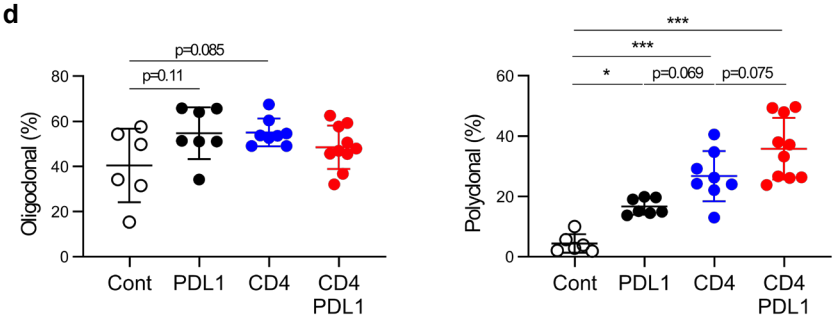
d
Oligoclonal (%)
p=0.085
p=0.11
Cont
PDL1
CD4
CD4
PDL1
Polyclonal (%)
***
***
*
p=0.069
p=0.075

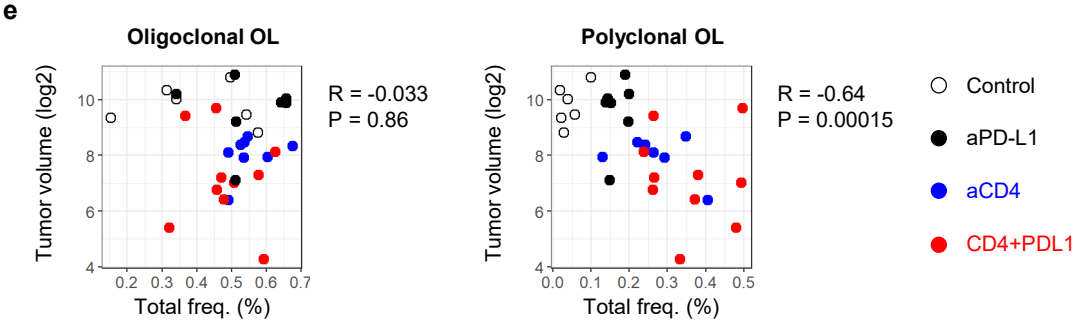
e
Oligoclonal OL
Tumor volume (log2)
Total freq. (%)
R = -0.033
P = 0.86
Polyclonal OL
R = -0.64
P = 0.00015
Control
aPD-L1
aCD4
CD4+PDL1

Figure 3

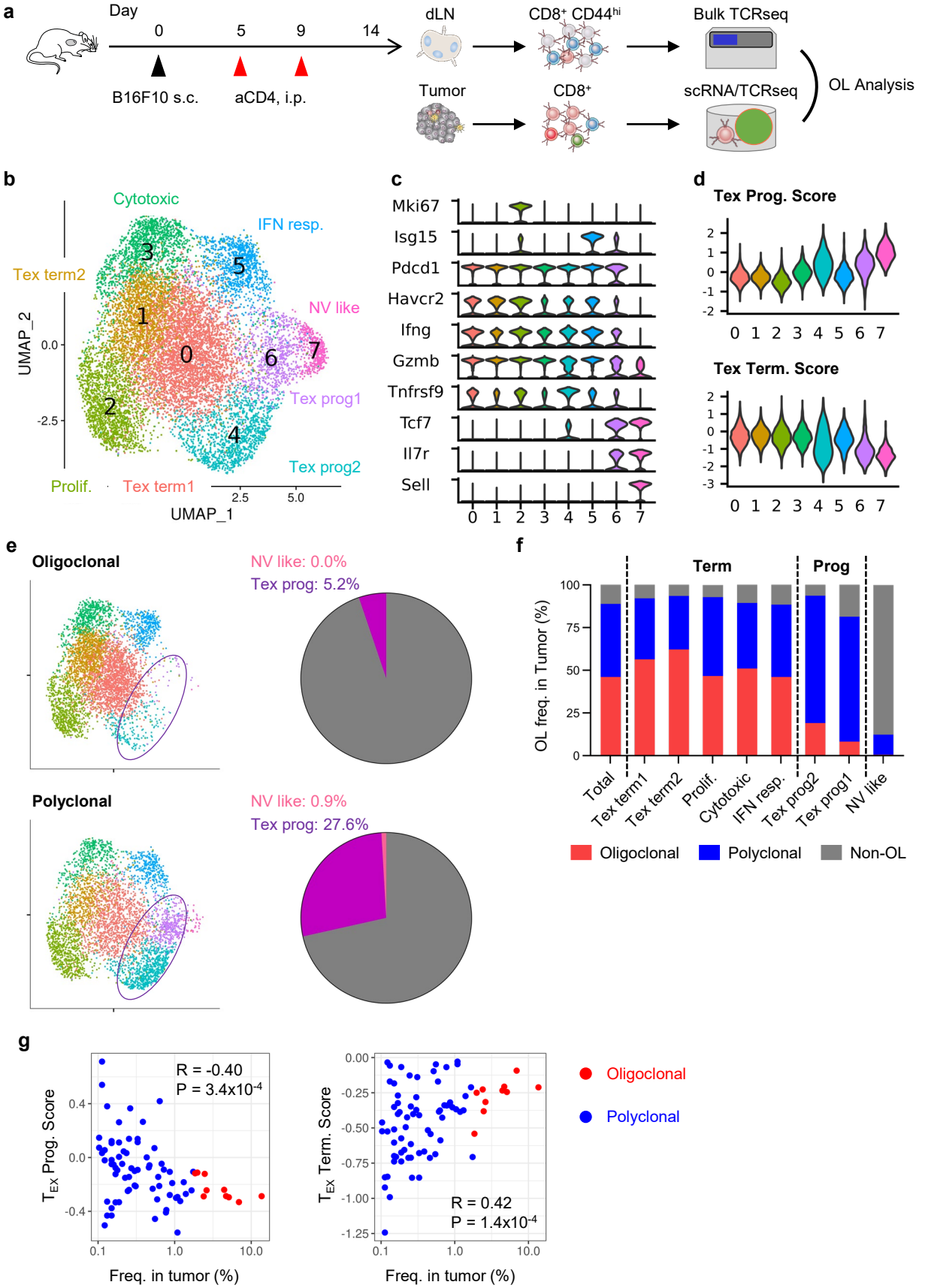
a
Day
0
5
9
14
B16F10 s.c.
aCD4, i.p.
dLN
CD8+ CD44hi
Bulk TCRseq
Tumor
CD8+
scRNA/TCRseq
OL Analysis
b
Cytotoxic
IFN resp.
Tex term2
NV like
Tex prog1
Tex prog2
Prolif.
Tex term1
UMAP_2
UMAP_1
c
Mki67
Isg15
Pdcd1
Havcr2
Ifng
Gzmb
Tnfrsf9
Tcf7
Il7r
Sell
d
Tex Prog. Score
Tex Term. Score
e
Oligoclonal
NV like: 0.0%
Tex prog: 5.2%
Polyclonal
NV like: 0.9%
Tex prog: 27.6%
f
Term
Prog
OL freq. in Tumor (%)
Total
Tex term1
Tex term2
Prolif.
Cytotoxic
IFN resp.
Tex prog2
Tex prog1
NV like
Oligoclonal
Polyclonal
Non-OL
g
R = -0.40
P = 3.4x10-4
TEX Prog. Score
Freq. in tumor (%)
R = 0.42
P = 1.4x10-4
TEX Term. Score
Freq. in tumor (%)
Oligoclonal
Polyclonal

Figure 4

a

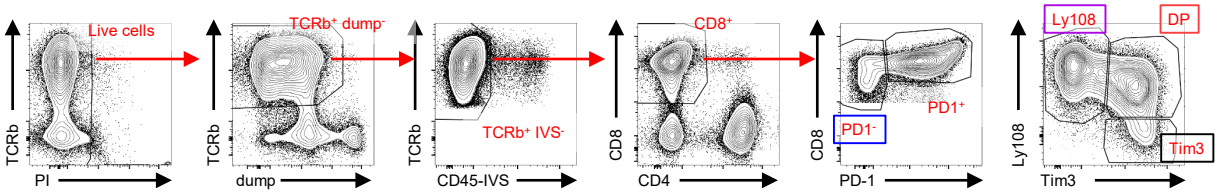

b

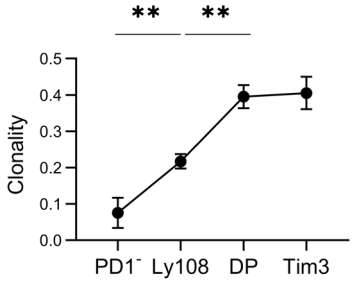

c

Subset	PD1-	Ly108	DP	Tim3	Pooled
Sorted cells	5,000	15,000	20,000	10,000	**50,000**
Freq. of clone A	0.04	0.2	0.02	0.01	**0.07**

Freq. in Pooled Tumor = (0.04 x 5000 + 0.2 x 15000 + 0.02 x 20000 + 0.01 x 10000) / 50000

d

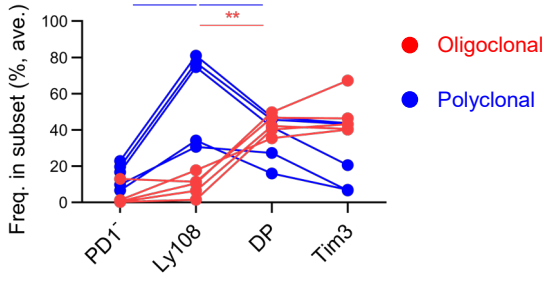

e

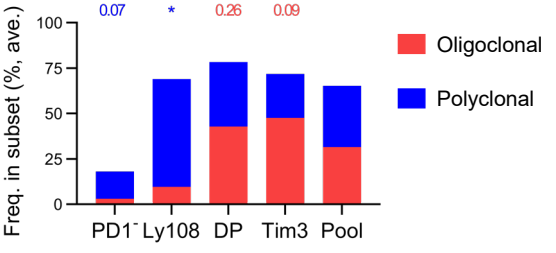

Figure 5

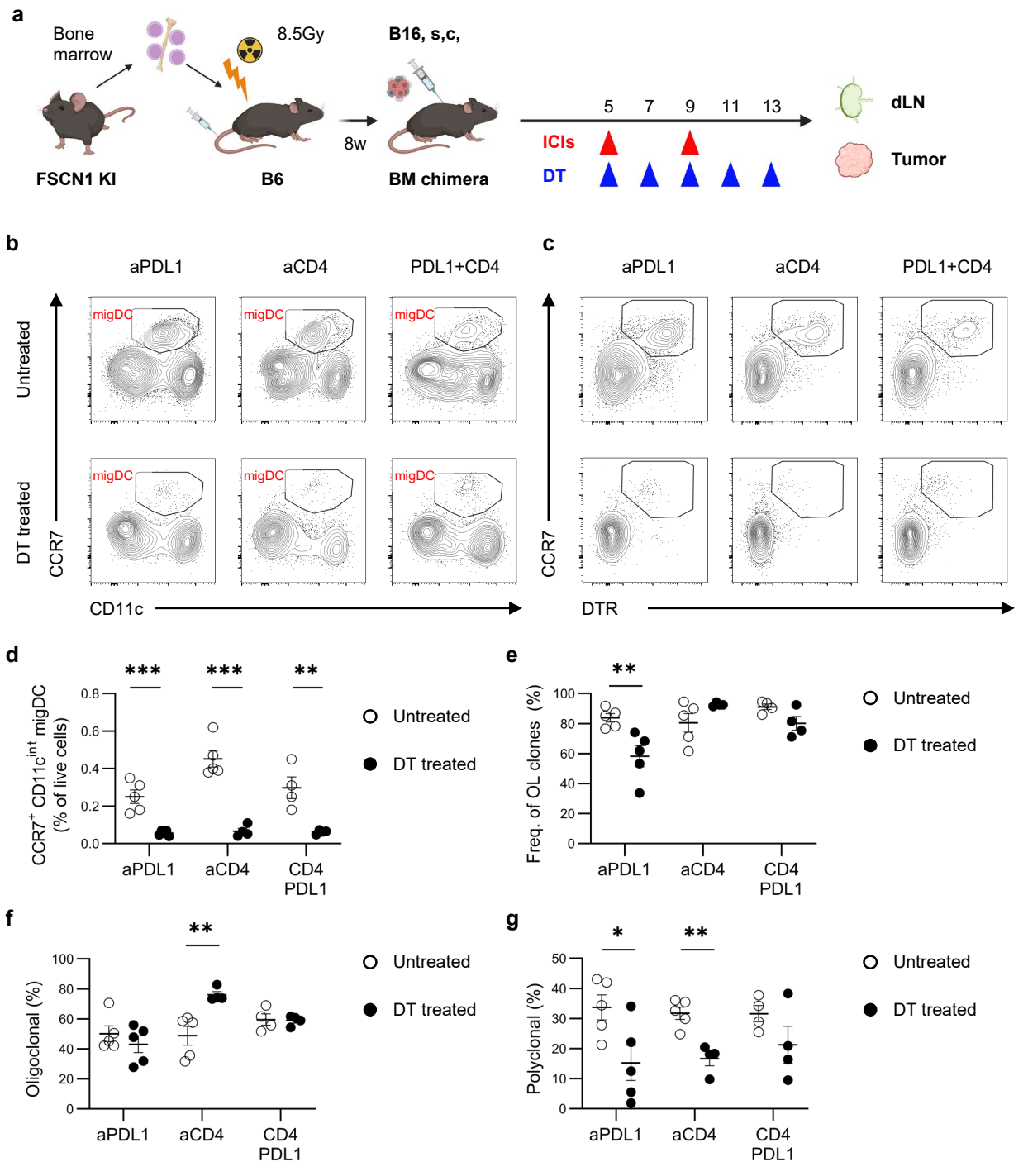
a
Bone marrow
8.5Gy
B16, s,c,
FSCN1 KI
B6
8w
BM chimera
5 7 9 11 13
ICIs
DT
dLN
Tumor
b
aPDL1
aCD4
PDL1+CD4
Untreated
DT treated
migDC
CCR7
CD11c
c
aPDL1
aCD4
PDL1+CD4
CCR7
DTR
d
CCR7+ CD11c int migDC (% of live cells)
aPDL1
aCD4
CD4 PDL1
Untreated
DT treated
e
Freq. of OL clones (%)
aPDL1
aCD4
CD4 PDL1
Untreated
DT treated
f
Oligoclonal (%)
aPDL1
aCD4
CD4 PDL1
Untreated
DT treated
g
Polyclonal (%)
aPDL1
aCD4
CD4 PDL1
Untreated
DT treated